Journal of Power Sources 203 (2012) 211–221

Contents lists available at SciVerse ScienceDirect

Journal of Power Sources

journal homepage: www.elsevier.com/locate/jpowsour

Modeling of reaction kinetics and transport in the positive porous electrode in a sodium–iron chloride battery

Damla Eroglu*, Alan C. West

Department of Chemical Engineering, Columbia University, 500 West 120th Street, Room 801, Mudd Building, New York, NY 10027, USA

ARTICLE INFO

Article history:
Received 2 September 2011
Received in revised form 1 November 2011
Accepted 2 November 2011
Available online 9 November 2011

Keywords:
Sodium–iron chloride battery
Mathematical modeling
Iron/iron chloride porous electrode
Iron chloride solubility
Reaction kinetics
Transport

ABSTRACT

A one-dimensional mathematical model of the positive electrode of a sodium–iron chloride battery for an isothermal, constant-current discharge–charge cycle is presented. Macroscopic theory of porous electrodes and concentrated solution theory are used in the model to describe the transport processes. The change in the solubility of $FeCl_2$ with position and time within the cell is included in the model by defining an equilibrium constant that is a function of the NaCl:$NaAlCl_4$ molar ratio. The concentrated solution theory for a three-ion system with common cation is extended to account for a diffusive flux of a sparingly soluble ferrous complex. It is seen that this flux is important, especially at moderate depths of discharge. The effect of the assumed solubility constant $K_{sp,FeCl}$ on the battery performance is characterized. When $K_{sp,FeCl}$ is higher than 10^6, its variation does not change the short-time behavior of the system appreciably. Simulations suggest that the iron accumulates near the sodium tetrachloroaluminate reservoir during discharge. When charging, the net movement is reversed. As a result of continuous cycling, simulations predict that iron is depleted at this boundary. For instance, at the end of the fifth cycle, the iron amount decreases by ~1% near the reservoir.

1. Introduction

A zebra battery is a high-temperature secondary battery system, with significant promise for high-energy density applications requiring long cycle life [1–12]. These battery systems also have zero self-discharge and are unaffected by the ambient temperature [7,11]. The zebra battery contains a liquid sodium electrode and a β″-alumina solid electrolyte, like the sodium–sulfur battery [1–12]. It also contains a second, molten salt electrolyte, sodium tetrachloroaluminate ($NaAlCl_4$), and a porous metal/metal chloride electrode [1–12]. The β″-alumina solid electrolyte only allows Na^+ ions to pass and it has essentially zero electronic conductivity [10–12]. The liquid electrolyte connects the ceramic electrolyte to the metal-chloride electrode for the rapid transport of Na^+ [1–12]. The battery operates in the range of 270–350 °C since high temperatures are needed to keep the sodium tetrachloroaluminate molten [1,4,11,12]. In addition, the resistance of the solid electrolyte is low in this temperature range [4,10–12].

Metal chloride cells are assembled in the discharged state by mixing the metal powder with NaCl in the positive electrode and adding the salt electrolyte as a dry powder to the mixture. After heating the cell to the operating temperature, it is then charged to generate the liquid sodium and metal chloride [5–9,12]. Iron chloride and nickel chloride are the most common electrodes used in these cells [1,3,4,12]. Here we treat the iron chloride electrode.

During discharge, sodium ions are conducted through the ceramic electrolyte from the negative electrode and then transferred to the positive electrode through sodium tetrachloroaluminate. Sodium reacts with iron chloride on the electrode to produce sodium chloride and iron. The battery is fully discharged when there is no iron chloride left in the cell [1–14]. The reverse of this process occurs during charging. The overall cell reaction is (1):

$$2Na + FeCl_2 \underset{\text{CHARGING}}{\overset{\text{DISCHARGING}}{\longleftrightarrow}} 2NaCl + Fe \quad (1)$$

with a thermodynamic cell potential of 2.35 V at 250 °C [1,2,4,7,12,15,16].

Sodium tetrachloroaluminate is a mixture of two binary molten salts, NaCl and $AlCl_3$, and the apparent concentration ratio of NaCl to $AlCl_3$ determines the solubility of $FeCl_2$ in the electrolyte [17]. NaCl-rich melts are typically used [14,15,17], in part because it is desirable to maintain low $FeCl_2$ solubility to minimize redistribution of active material. Nevertheless, the iron chloride is sparingly soluble, and with increased cycling, it does redistribute. The migration of the metal in the cell results in a loss in the performance of the battery, and may be a crucial failure mechanism [9,12,15,18,19].

In the literature, there are many studies of battery modeling [13,14,16,20–28]. Modeling of reaction kinetics and transport

* Corresponding author. Tel.: +1 212 854 4463; fax: +1 212 854 3054.
E-mail address: de2227@columbia.edu (D. Eroglu).

0378-7753/$ – see front matter © 2011 Elsevier B.V. All rights reserved.
doi:10.1016/j.jpowsour.2011.11.007

Nomenclature

a_m	specific surface area of Fe (cm^{-1})
a_s	specific surface area of $FeCl_2$ (cm^{-1})
c_A	concentration of $NaAlCl_4$ ($mol\,cm^{-3}$)
c_B	concentration of NaCl ($mol\,cm^{-3}$)
$c_{r,b}$	bulk concentration of ferrous complex ($mol\,cm^{-3}$)
$c_{r,e}$	equilibrium concentration of ferrous complex ($mol\,cm^{-3}$)
$c_{r,bsat}$	saturation bulk concentration of ferrous complex ($mol\,cm^{-3}$)
$c_{r,esat}$	saturation equilibrium concentration of ferrous complex ($mol\,cm^{-3}$)
$c_{r,s}$	surface concentration of ferrous complex ($mol\,cm^{-3}$)
c_T	total concentration ($mol\,cm^{-3}$)
D	diffusion coefficient of electrolyte ($cm^2\,s^{-1}$)
D_e	effective diffusion coefficient of electrolyte ($cm^2\,s^{-1}$)
F	Faraday's constant ($C\,mol^{-1}$)
H	height of the cell (cm)
I	apparent current density at separator ($A\,cm^{-2}$)
i_0	exchange current density ($A\,cm^{-2}$)
i_1	superficial current density in matrix phase ($A\,cm^{-2}$)
i_2	superficial current density in electrolyte phase ($A\,cm^{-2}$)
j	local transfer current ($A\,cm^{-3}$)
$K_{sp,FeCl}$	mole fraction equilibrium constant for the solubility of $FeCl_2$
$K_{sp,NaCl}$	solubility product of NaCl ($mol^2\,cm^{-6}$)
K_0, K_2, K_M	mole fraction equilibrium constants for $AlCl_3$–NaCl solvent equilibrium
k_m	mass transfer coefficient of ferrous complex between Fe and bulk ($cm\,s^{-1}$)
k_s	mass transfer coefficient of ferrous complex between $FeCl_2$ and bulk ($cm\,s^{-1}$)
k_p	rate constant for NaCl precipitation/dissolution reaction ($cm^3\,mol^{-1}\,s^{-1}$)
N_r	flux of ferrous complex ($mol\,cm^{-2}\,s^{-1}$)
R	gas constant ($J\,mol^{-1}\,K^{-1}$)
$R_{FeCl_2\,p}$	precipitation/dissolution rate of $FeCl_2$ ($mol\,cm^{-3}\,s^{-1}$)
$R_{NaCl\,p}$	precipitation/dissolution rate of NaCl ($mol\,cm^{-3}\,s^{-1}$)
r	radial distance from the center of current collector (cm)
r_0	outer radius of the current collector (cm)
r_A	outer radius of the separator (cm)
r_C	outer radius of the negative electrode (cm)
r_L	outer radius of the positive electrode (cm)
r_S	outer radius of the electrolyte reservoir (cm)
T	temperature (K)
t	time (s)
t_1^c	transference number of $AlCl_4^-$ relative to the common ion velocity
t_2^c	transference number of Cl^- relative to the common ion velocity
t_3^*	transference number of Na^+ relative to the molar-average velocity
$\bar{V}_A$	molar volume of molten $NaAlCl_4$ salt ($cm^3\,mol^{-1}$)
$\bar{V}_B$	molar volume of molten NaCl salt ($cm^3\,mol^{-1}$)
$\bar{V}_e$	molar volume of electrolyte ($cm^3\,mol^{-1}$)
$\bar{V}_{Fe}$	molar volume of Fe ($cm^3\,mol^{-1}$)
$\bar{V}_{FeCl_2}$	molar volume of $FeCl_2$ ($cm^3\,mol^{-1}$)
$\bar{V}_{NaCl}$	molar volume of NaCl precipitate ($cm^3\,mol^{-1}$)
V	cell potential (V)
V_{OC}	open-circuit cell potential (V)
v^*	molar-average electrolyte velocity ($cm\,s^{-1}$)
x_A	mole fraction of $NaAlCl_4$
x_{Asat}	saturation mole fraction of $NaAlCl_4$
x_B	mole fraction of NaCl
x_{AlCl_3}, $x_{Al_2Cl_6}$, $x_{Al_2Cl_7^-}$, $x_{Fe(AlCl_4)_4^{2-}}$	mole fractions of $AlCl_3$, Al_2Cl_6, $Al_2Cl_7^-$ and $Fe(AlCl_4)_4^{2-}$

Greek letters

α_a, α_c	anodic and cathodic transfer coefficients
γ_A	$NaAlCl_4$ activity coefficient
ε	porosity
ε_{Fe}	volume fraction of Fe
ε_{FeCl}	volume fraction of $FeCl_2$
ε_{NaCl}	volume fraction of NaCl precipitate
η	total overpotential (V)
κ	Electrolyte conductivity ($S\,cm^{-1}$)
κ_e	Electrolyte effective conductivity ($S\,cm^{-1}$)
σ	Iron conductivity ($S\,cm^{-1}$)
σ_e	Iron effective conductivity ($S\,cm^{-1}$)
ϕ_1	potential in matrix phase (V)
ϕ_2	potential in electrolyte phase (V)

processes in the cell is critical to predict the change of cell potential with the depth of discharge and to evaluate the outcomes of changes in design parameters [14,28]. Although there are many studies in the modeling of secondary lithium batteries [20–24], the modeling of sodium–metal chloride batteries is more limited [13,14,16,28]. Sudoh and Newman [14] discuss a very detailed model of a discharge–charge cycle of $Na/\beta''\text{-}Al_2O_3/NaAlCl_4/FeCl_2$ battery based on the macroscopic theory of porous electrodes [29] and concentrated solution theory [30]. In their model, the precipitation/dissolution rate of NaCl is taken into account. In addition, the mass transfer of the soluble ferrous complex is included in the electrode reaction rate [14], however they do not allow for redistribution within the cell via transport of the iron species through the electrolyte.

Bloom et al. [16] simulated the discharge of sodium–nickel chloride cells with a model that does not include the solubility of $NiCl_2$ and NaCl. Orchard and Weaving [28] also published a model on the discharge of sodium–iron chloride cells. In this study, the solubility of $FeCl_2$ and NaCl are not considered [28]. Vallance and White [13] modified Sudoh and Newman's model [14] and created a two-dimensional model for a fluted β″-alumina tube.

In this paper, a mathematical model of the porous cathode of a $Na/\beta''\text{-}Al_2O_3/NaAlCl_4/FeCl_2$ battery during a discharge–charge cycle is presented. The cathode is modeled using the macroscopic theory of porous electrodes [29]. Transport processes are modeled using Pollard and Newman's [30] concentrated-solution theory for a mixture of two binary molten salts in a porous electrode. Although the previous models are successful in defining the kinetics and transport in the cathode, none of them can predict the movement of the metal that takes place in the cell with increased cycling [9,12,15,18,19]. An advance offered by this model is that it accounts for the change in the solubility of $FeCl_2$ within the cell and predicts the relocation of the iron by modeling the transport assuming iron is dilute.

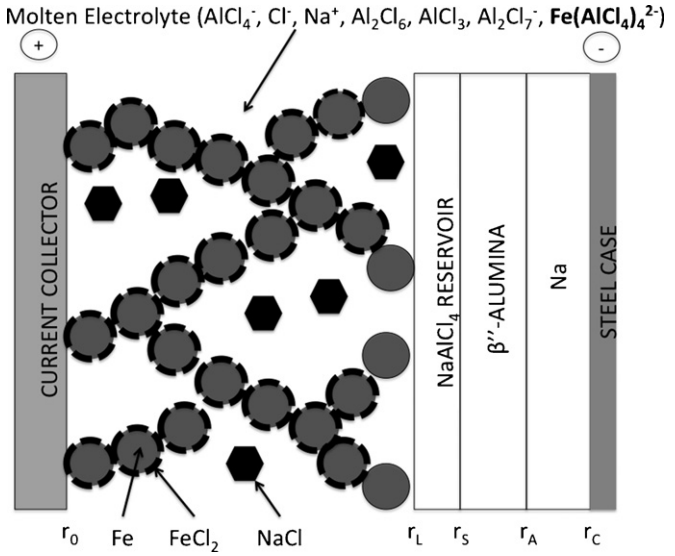

Fig. 1. Schematic diagram of the sodium–iron chloride battery in the model.

2. Model development

The isothermal, constant current discharge–charge of a Na-$FeCl_2$ battery is represented using a one-dimensional, cylindrical model. As seen in Fig. 1, the cell is composed of six parts: the cathode current collector ($r < r_0$), the positive porous Fe/$FeCl_2$ electrode (between r_0 and r_L), the sodium tetrachloroaluminate reservoir (between r_L and r_S), the β″-alumina solid electrolyte (between r_S and r_A), the negative liquid sodium electrode (between r_A and r_C) and the anode current collector [14]. In this study, only the positive porous electrode is modeled.

The positive porous electrode (between r_0 and r_L) is composed of a matrix, which consists of NaCl crystals and porous iron particles partially coated with $FeCl_2$, and a molten electrolyte, a mixture of $AlCl_3$ and NaCl. Transport equations are derived from Pollard and Newman's [30] study for a mixture of two binary molten salts with a common ion in a porous electrode. As in their study, A and B are used for $NaAlCl_4$ and NaCl salts and 1, 2 and 3 are used for $AlCl_4^-$, Cl^- and Na^+ ions, respectively.

The electrolyte is a concentrated solution of $AlCl_4^-$, Cl^- and Na^+ [30]. From solvent-equilibria studies of $AlCl_3$–NaCl melts, it is known that the electrolyte also contains Al_2Cl_6, $AlCl_3$ and $Al_2Cl_7^-$ ions in low concentrations [31]. In addition to these ions, there is the soluble ferrous complex, most probably in the form of $Fe(AlCl_4)_4^{2-}$ [14,17]. The concentrations of this ferrous complex on $FeCl_2$ and Fe surfaces and in the bulk may not be the same depending on the interfacial reaction rates. The schematic diagram of the Fe/$FeCl_2$ electrode defining the equilibrium, bulk and surface concentrations of the soluble ferrous complex can be seen in Fig. 2.

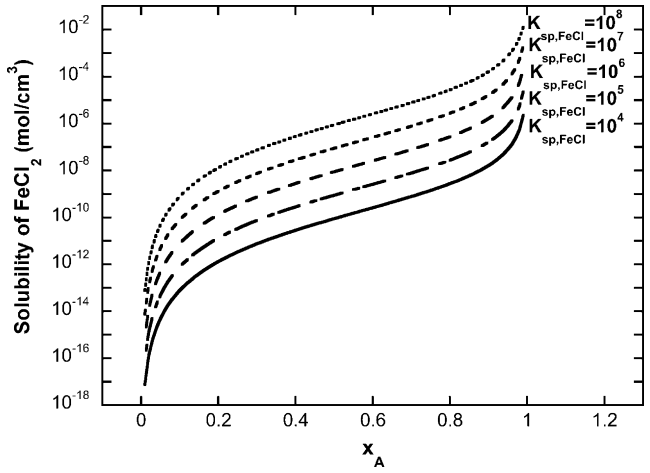

Fig. 3. Solubility of $FeCl_2$, $c_{r,e}$, as a function of $NaAlCl_4$ mole fraction, x_A, for different values of $K_{sp,FeCl}$ in a semi-log plot.

2.1. Solubility of $FeCl_2$

The equilibrium concentration of the complex on the $FeCl_2$ surface is dictated by the solubility of $FeCl_2$. In the previous models [13,14], it was assumed that the solubility concentration of iron chloride, $c_{r,e}$, is constant within the cell. In this model, we allow it to change within the cell as a function of radial position and time.

In a previous study [28], the solvent equilibrium of $AlCl_3$–NaCl melts is described, and three mole fraction equilibrium constants, K_0, K_2, and K_M were found. In this study, another equilibrium constant, $K_{sp,FeCl}$, is defined for the solubility of $FeCl_2$. Therefore, the equilibrium is now defined with the reactions (2)–(5):

$$2AlCl_{3(l)} \leftrightarrow Al_2Cl_{6(l)} \quad K_0 \tag{2}$$

$$AlCl_4^- + AlCl_3 \leftrightarrow Al_2Cl_7^- \quad K_2 \tag{3}$$

$$2AlCl_4^- \leftrightarrow Al_2Cl_7^- + Cl^- \quad K_M \tag{4}$$

$$FeCl_{2(s)}^- + 2Al_2Cl_7^- \leftrightarrow Fe(AlCl_4)_4^{2-} \quad K_{sp,FeCl} \tag{5}$$

The solubility of $FeCl_2$, $c_{r,e}$, which is determined by these four equilibrium reactions, is only a function of the $NaAlCl_4$ mole fraction, x_A, and the assumed solubility constant, $K_{sp,FeCl}$. In Fig. 3, the solubility as a function of x_A is shown for $K_{sp,FeCl}$ values between 10^4 and 10^8. It can be seen that, as $K_{sp,FeCl}$ increases, the solubility of $FeCl_2$ also increases. The model predicts a significant change in the solubility, especially for x_A values between 0.6 and 0.9. The assumed relationships for $c_{r,e}$ are given in Appendix A.

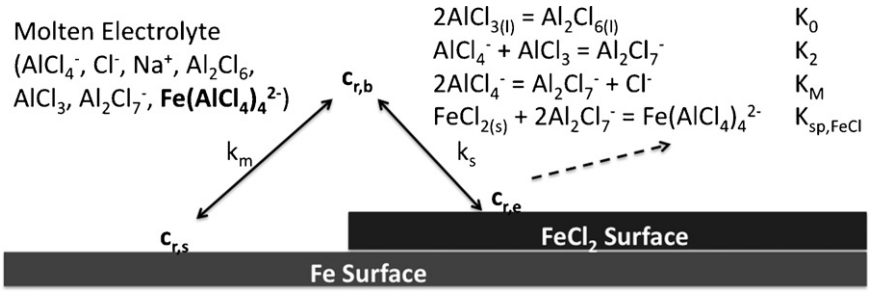

Fig. 2. Schematic diagram of the Fe/$FeCl_2$ electrode showing the equilibrium ($c_{r,e}$), bulk ($c_{r,b}$) and surface ($c_{r,s}$) concentrations of the soluble ferrous complex, $Fe(AlCl_4)_4^{2-}$.

2.2. Concentration of the soluble ferrous complex in the electrolyte

The redistribution of iron in the cell as a result of cycling indicates there is a movement of the soluble ferrous complex within the cell. For this reason, the flux of $Fe(AlCl_4)_4^{2-}$ was included in the model. The electrolyte is a concentrated solution composed of $AlCl_4^-$, Cl^-, Na^+, Al_2Cl_6, $AlCl_3$, $Al_2Cl_7^-$ and $Fe(AlCl_4)_4^{2-}$ ions. Since the concentration of the species 1, 2 and 3 are very high compared to the other ions, in the derivation of the flux equation for the ferrous complex, the presence of Al_2Cl_6, $AlCl_3$ and $Al_2Cl_7^-$ ions were neglected. Thus the multicomponent diffusion equation [32] for the ferrous complex, Eq. (6), only contains species 1, 2, 3 and the ferrous complex, denoted with the subscript r:

$$c_{r,b}\nabla\mu_r = \frac{RT}{c_T}\left(\frac{c_{r,b}c_1}{D_{r1}}(v_1 - v_r) + \frac{c_{r,b}c_2}{D_{r2}}(v_2 - v_r) + \frac{c_{r,b}c_3}{D_{r3}}(v_3 - v_r)\right) \quad (6)$$

where μ_r is the electrochemical potential of the ferrous complex, c_T is the total concentration, $c_{r,b}$, c_1, c_2 and c_3 are the concentrations of the species and v_r, v_1, v_2 and v_3 are the velocities of the species.

Since we do not have independent measurement of the diffusion coefficients of the species, D_{ri}, we assume $D_{r1} = D_{r2} = D_{r3} = D_e$. Also since $c_{r,b} \ll c_1$, c_2 and c_3, we assume:

$$c_T \approx c_1 + c_2 + c_3 \quad (7)$$

and

$$c_T v^* \approx N_1 + N_2 + N_3 \quad (8)$$

where v^* is the molar-average velocity and N_1, N_2 and N_3 are the fluxes of the species.

With these assumptions, Eq. (6) is rewritten to give the flux of ferrous complex, N_r:

$$N_r = c_{r,b}v_r = -\frac{D_e}{RT}c_{r,b}\nabla\mu_r + c_{r,b}v^* \quad (9)$$

Inserting the Gibbs–Duhem equation, using the definition of the effective diffusion coefficient of the electrolyte, $D_e = D\varepsilon^{1.5}$, and neglecting electrical migration since the transference number of the iron species is essentially zero, Eq. (10) is obtained:

$$N_r = -D\varepsilon^{1.5}\nabla c_{r,b} + c_{r,b}v^* \quad (10)$$

A material balance of the soluble ferrous complex in the electrolyte enables calculation of the bulk concentration of $Fe(AlCl_4)_4^{2-}$, $c_{r,b}$. When the quasi steady-state assumption is applied, the mass transfer rate of ferrous complex from the $FeCl_2$ surface to the bulk is equal to the flux of ferrous complex in the electrolyte and the electrochemical reaction rate. The material balance for $c_{r,b}$ is shown in Eq. (11):

$$0 = -\nabla \cdot N_r + \frac{j}{2F} + k_s a_s(c_{r,e} - c_{r,b}) \quad (11)$$

where j is the local transfer current, k_s is the mass transfer coefficient of ferrous complex between $FeCl_2$ and bulk and a_s is the specific surface area of $FeCl_2$.

2.3. Concentration of the soluble ferrous complex on the Fe surface

The surface concentration, $c_{r,s}$, is calculated by equating the mass transfer rate of ferrous complex from the bulk to the Fe surface to the electrochemical reaction rate as given in Eq. (12):

$$\frac{j}{2F} = -k_m a_m(c_{r,b} - c_{r,s}) \quad (12)$$

where k_m is the mass transfer coefficient of ferrous complex between Fe and bulk and a_m is the specific surface area of Fe.

2.4. Reduction/oxidation reaction rate

The reaction that takes place at the cathode is shown in Eq. (13):

$$FeCl_{2(s)} + 2e^- \leftrightarrow Fe_{(s)} + 2Cl^- \quad (13)$$

The reaction rate accounts for the mass transfer of ferrous complex from the bulk to the Fe surface as described in Eq. (14). This rate expression is a modification of Eq. (12) in Ref. [14], with the appropriate changes for estimation of $c_{r,e}$ and $c_{r,b}$. All the other mass transfer rates and areas are the same with the previous studies [13,14].

$$j = \frac{\exp((\alpha_a F/RT)\eta) - ((c_{r,b}/c_{r,e})\exp(-(\alpha_c F/RT)\eta))}{(1/i_0 a_m) + (1/2Fc_{r,e})\left(1/k_m a_m\right)\exp(-(\alpha_c F/RT)\eta)} \quad (14)$$

where the total overpotential, η, is given by:

$$\eta = \phi_1 - \phi_2 \quad (15)$$

At any point in the cell where the volume fraction of iron chloride is zero during the discharge, the transfer current is set to zero.

2.5. Precipitation rate of NaCl

The second reaction taking place inside the porous cathode is the precipitation/dissolution reaction of NaCl, which is given by Eq. (16). The rate of this reaction is shown in Eq. (17) [14]. When x_A is equal to its saturation value, the rate is equal to zero. When it is lower than the saturation value, $R_{NaCl\ p}$ is positive indicating there is precipitation of NaCl in the cell.

$$Na^+ + Cl^- \leftrightarrow NaCl_{(s)} \quad (16)$$

$$R_{NaCl\ p} = k_p\left(\frac{1 - x_A}{\bar{V}_e^2} - K_{sp,NaCl}\right) \quad (17)$$

where the average molar volume of the electrolyte, $\bar{V}_e$:

$$\bar{V}_e = \left(\bar{V}_A - \bar{V}_B\right)x_A + \bar{V}_B \quad (18)$$

2.6. Precipitation rate of $FeCl_2$

The precipitation rate of iron chloride is given by:

$$R_{FeCl_2\ p} = -k_s a_s(c_{r,e} - c_{r,b}) \quad (19)$$

The precipitation/dissolution rate is zero when the equilibrium and bulk concentrations of the ferrous complex are equal to each other. The rate is positive showing there is precipitation of $FeCl_2$ when the bulk concentration of the ferrous complex is higher than its equilibrium concentration.

2.7. Material balances on iron, iron chloride and sodium chloride

The equations used for the calculation of the volume fractions of iron, iron chloride and sodium chloride are shown in Eqs. (20), (21) and (22), respectively. The total solids porosity, ε, given in Eq. (23) is calculated based on the fact that the summation of the porosity and the volume fraction of the matrix is equal to 1.

$$\frac{\partial\varepsilon_{Fe}}{\partial t} = -\frac{\bar{V}_{Fe}}{2F}j \quad (20)$$

$$\frac{\partial\varepsilon_{FeCl_2}}{\partial t} = \bar{V}_{FeCl_2}R_{FeCl_2\ p} \quad (21)$$

$$\frac{\partial\varepsilon_{NaCl}}{\partial t} = \bar{V}_{NaCl}R_{NaCl\ p} \quad (22)$$

$$\frac{\partial\varepsilon}{\partial t} = \frac{\bar{V}_{Fe}}{2F}j - \bar{V}_{NaCl}k_p\left(\frac{1 - x_A}{\bar{V}_e^2} - K_{sp,NaCl}\right) + \bar{V}_{FeCl_2}k_s a_s(c_{r,e} - c_{r,b}) \quad (23)$$

2.8. Material balance on electrolyte

The mole fraction of $NaAlCl_4$, x_A, is the variable in the model used to set the composition of the electrolyte. A material balance is the same as given in Ref. [13]:

$$\varepsilon\frac{\partial x_A}{\partial t} = \bar{V}_e x_A R_{NaCl\,p} + \bar{V}_e x_A \frac{j}{F} - v^*\nabla x_A + \nabla\cdot(D\varepsilon^{1.5}\nabla x_A) - D\varepsilon^{1.5}\frac{\bar{V}_A - \bar{V}_B}{\bar{V}_e}(\nabla x_A)^2 + \frac{\bar{V}_e i_2}{2F}\nabla x_A \quad (24)$$

2.9. Current densities in electrolyte and matrix phases

Ohm's law is used to define the current densities in the matrix and electrolyte phases, i_1 and i_2, that are shown in Eqs. (25) and (26), respectively [13,14,30]. The summation of these two variables is equal to the apparent current density, I (measured at r_S) at any point in the cathode [14]. Effective conductivities of the metal and electrolyte are defined as $\sigma_e = \sigma\varepsilon^{1.5}$ and $\kappa_e = \kappa\varepsilon^{1.5}$ [13,14]. In the derivations, the transference number of sodium ion, t_3^* is assumed to be 0.5 since the sodium–ion concentration is half of the total concentration, and t_1^c and t_2^c are taken as x_A and x_B, respectively [14].

$$i_1 = -\sigma_e\nabla\phi_1 \quad (25)$$

$$i_2 = \frac{\sigma_e\kappa_e}{\sigma_e+\kappa_e}\left\{\nabla\eta + \frac{r_S I}{\sigma_e r} + \frac{RTt_1^c}{F(1-x_A)x_A}\left(1+\frac{d\ln\gamma_A}{d\ln x_A}\right)\nabla x_A\right\} \quad (26)$$

$$i_1 + i_2 = \frac{Ir_S}{r} \quad (27)$$

where ϕ_1 is the potential in the matrix phase and γ_A is the activity coefficient.

2.10. Local transfer current

The definition of the local transfer current is [13,14]:

$$j = \nabla\cdot i_2 \quad (28)$$

2.11. Molar average velocity

The change in the porosity with time and position creates a velocity field inside the cell, which is given in Eq. (29) [13,14]. This velocity within the cell results in the convective mass transfer of the species, therefore it must be considered in the model.

$$\nabla\cdot v^* = -\frac{\bar{V}_{Fe}+2\bar{V}_B}{2F}j + \left(\bar{V}_{NaCl}-\bar{V}_B\right)R_{NaCl\,p} + \left(\bar{V}_A-\bar{V}_B\right)\nabla\cdot[D\varepsilon^{1.5}(c_A+c_B)\nabla x_A] + \frac{\bar{V}_A}{F}\nabla\cdot(t_1^* i_2) - \frac{\bar{V}_B}{F}\nabla\cdot(t_2^* i_2) - \bar{V}_{FeCl_2}k_s a_s(c_{r,e}-c_{r,b}) \quad (29)$$

2.12. Total iron amount

In order to describe the movement of the iron in the cell, a parameter for the total iron amount is used to show iron redistribution within the battery:

$$\text{Total}_{Iron} = \frac{\varepsilon_{Fe}}{\bar{V}_{Fe}} + \frac{\varepsilon_{FeCl_2}}{\bar{V}_{FeCl_2}} + c_{r,b} \quad (30)$$

2.13. Cell potential

One of the most important features of battery modeling is the prediction of the external cell potential. Ref. [14] discusses the calculation of the terminal voltage in detail. In this paper, a simplified version of their equation is used under the assumptions of constant reservoir and ceramic electrolyte resistances and constant negative electrode overpotential. With these assumptions, the change in potential with time can simply be calculated using:

$$V = V_{OC} + (\phi_1)_{r=r_0} - (\phi_2)_{r=r_L} + \left(\frac{RT}{F}\ln\frac{1-x_{Asat}}{1-x_A}\right)_{r=r_L} \quad (31)$$

where V_{OC} is the open-circuit cell potential and ϕ_1 and ϕ_2 are the potentials in the matrix and electrolyte phases, respectively.

2.14. Initial conditions

Since the cell is fully charged before the first discharge, the initial conditions for ε, ε_{Fe}, ε_{FeCl} and ε_{NaCl}, are 0.546, 0.184, 0.26 and 0.01, respectively [13,14]. For the mole fraction of A, x_A, the saturation value of 0.8972 [13] is used. It is assumed that j is constant throughout the cell initially, and the initial conditions for the other 5 variables, Φ_1, Φ_2, i_1, i_2 and η, are calculated using this assumption. Finally, Eq. (32), which is derived using the fluxes of species 1, 2 and 3, is used for the initial condition of v^* [14].

$$v^* = \frac{\bar{V}_e - 2\bar{V}_B - \bar{V}_{Fe} + \bar{V}_{FeCl_2}}{2F}i_2 \quad (32)$$

2.15. Boundary conditions

The boundary conditions at r_0 are given in Eqs. (33)–(39):

$$i_2 = 0 \quad (33)$$

$$i_1 = \frac{Ir_s}{r_0} \quad (34)$$

$$\nabla\Phi_2 = 0 \quad (35)$$

$$\nabla\eta = -\frac{r_s I}{\sigma_e r_0} \quad (36)$$

$$\nabla x_A = 0 \quad (37)$$

$$v^* = 0 \quad (38)$$

$$\nabla c_{r,b} = 0 \quad (39)$$

The boundary conditions at r_L are:

$$i_2 = \frac{Ir_s}{r_L} \quad (40)$$

$$i_1 = 0 \quad (41)$$

$$\Phi_1 = 0 \quad (42)$$

$$\nabla x_A = 0 \quad (43)$$

$$v^* = \frac{\bar{V}_e - 2\bar{V}_B - \bar{V}_{Fe} + \bar{V}_{FeCl_2}}{2F}i_2 \quad (44)$$

$$\nabla c_{r,b} = 0 \quad (45)$$

The 14 variables in the model, Φ_1, Φ_2, i_1, i_2, j, η, x_A, ε, ε_{Fe}, ε_{FeCl}, ε_{NaCl}, v^*, $c_{r,e}$ and $c_{r,b}$, are calculated solving the Eqs. (11), (14), (15), (20)–(29) and (A6) using a block tri-diagonal matrix algorithm in FORTRAN [32]. The simulations were carried out with 501 node points and time-step sizes of 20.61 s during discharge and 9 s during charge. For continuous cycling, time-step sizes of 6 s and 9 s are used for discharge and charge, respectively. In order to test the convergence, time-step size was halved, resulting in negligible changes in the results. In a similar manner, doubling of node points did not change the results to any appreciable extent.

Table 1
Parameters in the model.

r_0	0.25 cm
r_L	2.5 cm
r_{Middle}	1.3705 cm
r_S	2.8 cm
H	30 cm
T	573 K
I	$-30\,mA\,cm^{-2}$ discharge/$10\,mA\,cm^{-2}$ charge
$\bar{V}_{Fe}$	$7.1\,cm^3\,mol^{-1}$
$\bar{V}_{FeCl_2}$	$40.1\,cm^3\,mol^{-1}$
$\bar{V}_{NaCl}$	$27.0\,cm^3\,mol^{-1}$
$\bar{V}_A$	$121.6\,cm^3\,mol^{-1}$
$\bar{V}_B$	$37.06\,cm^3\,mol^{-1}$
k_p	$0.1\,cm^3\,mol^{-1}\,s^{-1}$
$K_{sp,NaCl}$	$8.06\times10^{-6}\,mol^2\,cm^{-6}$
$\alpha_a=\alpha_c$	1
D	$5.135\times10^{-6}\,cm^2\,s^{-1}$
σ	$3.5\times10^4\,S\,cm^{-1}$
K_0	3.85×10^5
K_2	10^3
K_M	2.37×10^{-6}
V_{OC}	2.32 V

3. Results and discussion

Results are discussed assuming an operating temperature of 300 °C. The values of parameters used in the simulations are shown in Table 1. Most of these values are taken from previous work for sodium–iron chloride battery modeling [13,14,31]. For the electrical conductivity and activity coefficient equations, the equations in the Appendix of Ref. [14] were used. The full discharge time is calculated as 46,040 s (12.8 h) with $-30\,mA\,cm^{-2}$ constant current discharging and the depth of discharge (DOD) is computed as the ratio of the actual discharge time to the full discharge time. The charge time is taken as 18,000 s (5 h) in the simulations. In all of the results given for the model, $K_{sp,FeCl}$ is taken as 10^6, unless otherwise stated.

3.1. Solubility of $FeCl_2$ and bulk concentration of the ferrous complex

The change in iron chloride volume fraction, $NaAlCl_4$ mole fraction and solubility of $FeCl_2$ within the cell during discharge can be seen in Figs. 4–6, respectively. Initially (DOD = 0), the solubility is constant along the cell since x_A is equal to its saturation value at every point in the cell. With increasing time (DOD = 0.2), the solubility begins to decrease at the electrode–reservoir interface, r_L. This is expected since x_A has the same trend at DOD = 0.2 (Fig. 5) with the minimum value at r_L. For larger discharge times (DOD = 0.7 and 0.9), the minimum value of x_A shifts inward to r_0 (Fig. 5) and the solubility decreases throughout the cell with the same trend (Fig. 6).

The bulk concentration of the ferrous complex with respect to position and time is shown in Fig. 7. As it can be seen in the figure, at low discharge times (DOD = 0.2) the bulk concentration follows the equilibrium concentration; it decreases with increasing r. As discharge time increases (DOD = 0.7), although iron chloride is depleted near the electrode–reservoir interface (Fig. 4), the concentration of the soluble ferrous complex in the electrolyte is not zero. This result shows that the flux of the ferrous complex becomes more significant with increasing depth of discharge in part because $FeCl_{2(s)}$ is no longer present to buffer variations in the bulk iron concentration. As the discharge time increases further (DOD = 0.9),

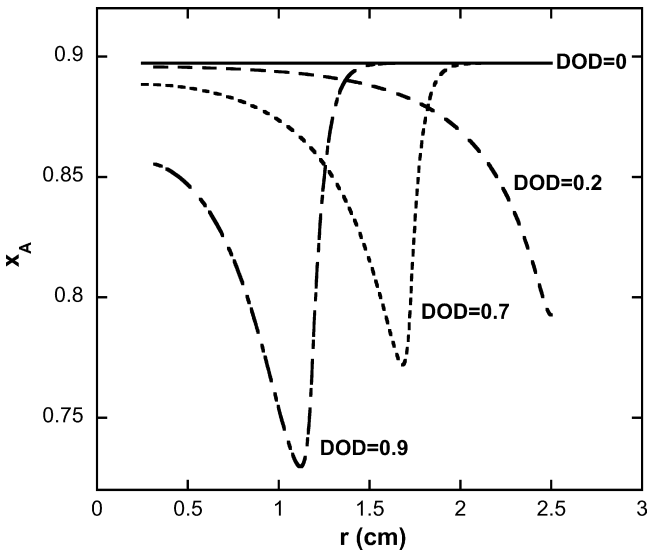

Fig. 5. The change of $NaAlCl_4$ mole fraction, x_A, with radial position at different DODs during discharge ($K_{sp,FeCl} = 10^6$).

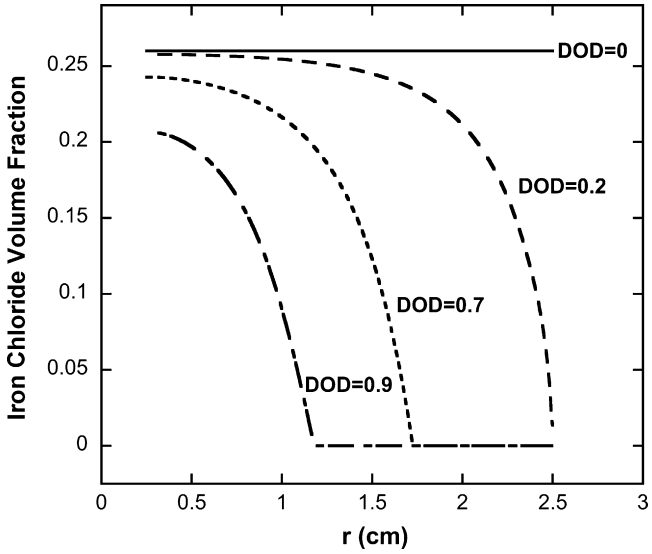

Fig. 4. The change of iron chloride volume fraction, ε_{FeCl}, with radial position at different DODs during discharge ($K_{sp,FeCl} = 10^6$).

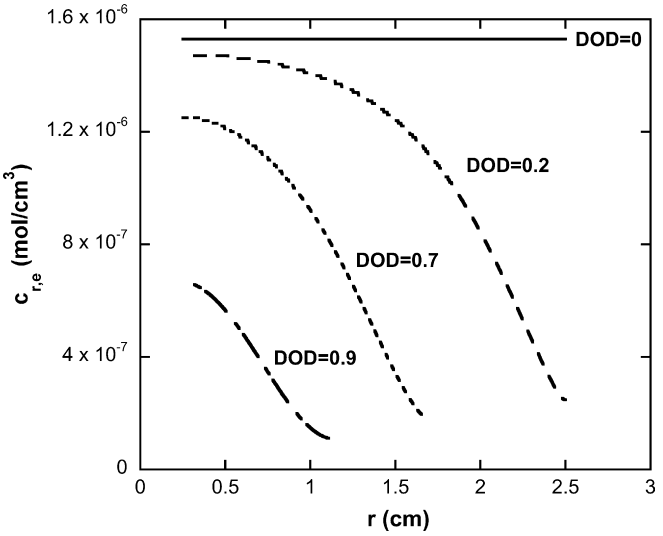

Fig. 6. The change of solubility of $FeCl_2$, $c_{r,e}$, with radial position at different DODs during discharge ($K_{sp,FeCl} = 10^6$).

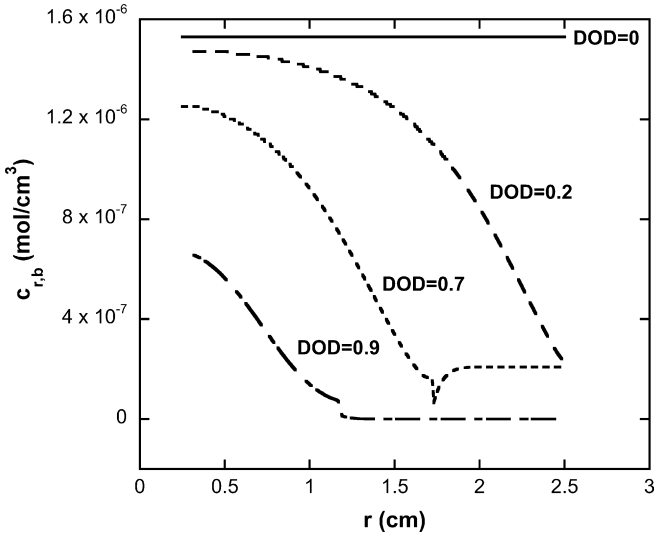

Fig. 7. The change of bulk concentration of ferrous complex, $c_{r,b}$, with radial position at different DODs during discharge ($K_{sp,FeCl} = 10^6$).

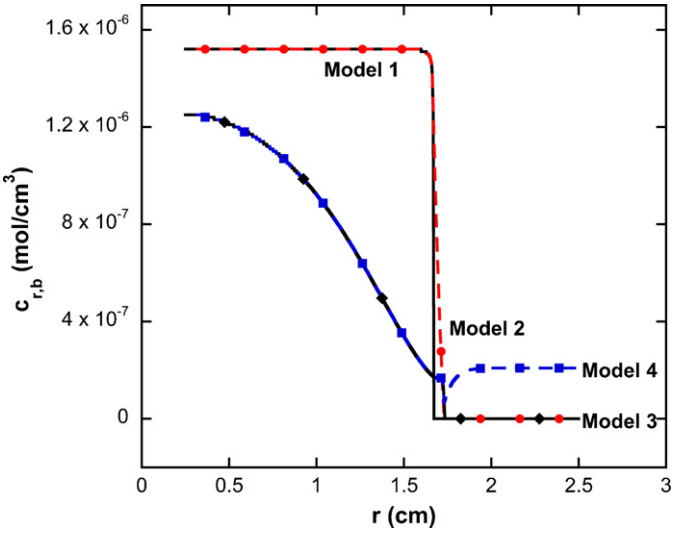

Fig. 9. Comparison of bulk concentration results for the complete model (model 4 – flux, variable solubility) and different simplifications (model 1 – no flux, constant solubility), (model 2 – flux, constant solubility), (model 3 – no flux, variable solubility). For all cases DOD = 0.7 and $K_{sp,FeCl} = 10^6$.

the electrolyte concentration of iron approaches zero near the r_L boundary. At this high depth of discharge, iron chloride is depleted in the majority of the cell (Fig. 4), and the electrolyte concentration of the ferrous complex is very low, even near r_0. Therefore, the flux of the ferrous complex is negligibly small; it is not enough to create non-zero bulk concentrations near r_L. The discontinuities seen in Fig. 7 (DOD = 0.7 and 0.9) occur at the points where the iron chloride phase is calculated to disappear. We have confirmed that the discontinuities do not propagate numerical errors.

3.2. Relocation of iron within the cell

The change in the total iron amount at r_0, r_{Middle} and r_L during a discharge–charge cycle is shown in Fig. 8. In the figure, it can be seen that there is a sudden increase in the total iron amount at r_L during the early stages of discharge. This increase in total iron amount can be explained by a sharp increase in Fe concentration. This sharp increase shows that there is a significant flux of the ferrous complex present towards r_L during the early stages of the discharge. After this initial increase, the total iron content does not change at r_L until the end of discharge. As the iron chloride is depleted near r_L, the reaction front migrates inward towards r_0, and the increase in Fe

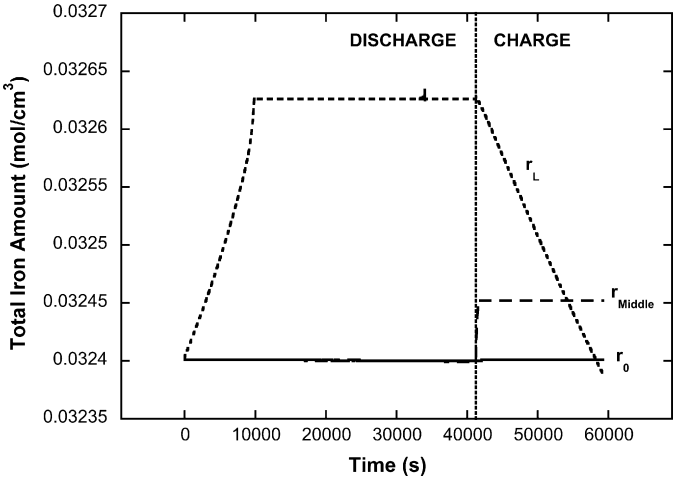

Fig. 8. The change of total iron amount with time at different radial positions ($K_{sp,FeCl} = 10^6$).

concentration also ends. This suggests that unlike the initial stages, the flux of the ferrous complex is not enough to create a change in Fe concentration or total iron amount. As discharge proceeds, $c_{r,b}$ also goes to zero and the total iron amount reflects only the Fe concentration at r_L. At r_{Middle} and r_0, the iron amount decreases slightly during discharge. These results show that there is a net flux of ferrous complex from r_0 to r_L. The flux of the ferrous complex is reversed during charging of the cell, causing the total iron amount to decrease at r_L and increase at r_{Middle} and r_0. As a result of a discharge–charge cycle, the total amount of iron is reduced slightly at r_L. This small change in the total iron amount as a result of one cycle may become significant after several dozen cycles.

3.3. Significance of solubility of $FeCl_2$ variation and flux of the ferrous complex in the model

In order to examine the role of the iron chloride solubility change and ferrous complex flux in the prediction of iron redistribution inside the cell, four model predictions are compared. In the first model, the solubility of iron chloride is constant throughout the cell at its saturation value. In addition, the flux of the ferrous complex is not included in the material balance of the ferrous complex in the bulk. This first model is essentially identical to Sudoh and Newman's model [13,14]. In the second model, the solubility of iron chloride is constant throughout the cell, but the flux of the ferrous complex is included. In the third model, the variation in $FeCl_2$ solubility is taken into account, but the flux is not included. Finally, the fourth model is the one described in this paper; counting for both the solubility change and ferrous complex flux inside the cell. In order to compare these four models, the bulk concentration profile at DOD = 0.7 is chosen as shown in Fig. 9.

When the models with no flux (models 1 and 3) are compared with the models accounting for the flux of the ferrous complex (models 2 and 4) in Fig. 9, it can be seen that the presence of the flux in the model resulted in prediction of higher bulk concentrations near the r_L boundary. For instance, the bulk concentration is non-zero for model 4 near the r_L boundary although it is zero for model 3. From these results it can be concluded that the effect of the flux of the ferrous complex is significant at moderate DODs near r_L, where iron chloride is depleted.

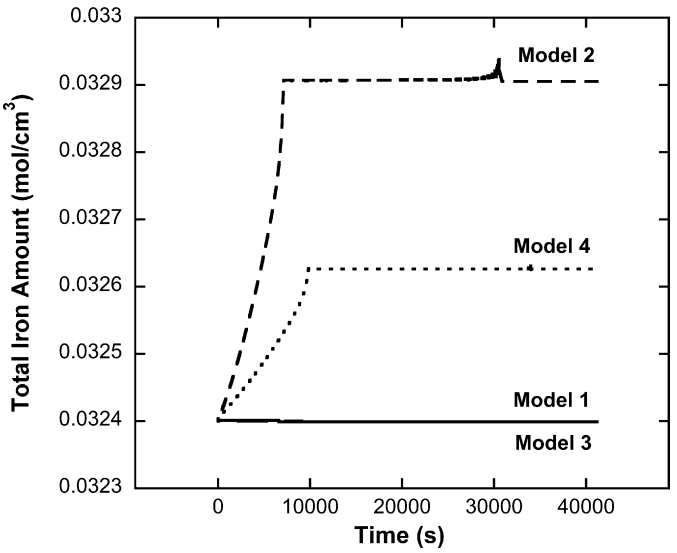

Fig. 10. Comparison of total iron amount results for the complete model (model 4 – flux, variable solubility) and different simplifications (model 1 – no flux, constant solubility), (model 2 – flux, constant solubility), (model 3 – no flux, variable solubility). For all cases DOD = 0.7 and $K_{sp,FeCl} = 10^6$.

The effect of variation of $FeCl_2$ solubility on the electrolyte concentration is also apparent in Fig. 9, especially near r_0, where solid iron chloride is still present. Electrolyte concentration does not change near r_0 for the models with constant solubility (models 1 and 2) whereas it decreases with radial distance for models with variable solubility (models 3 and 4). The variation in $c_{r,e}$ results in lower electrolyte concentrations near this boundary.

In Fig. 10, the total iron amount at r_L as a function of discharge time for these four models are compared. This figure clearly displays the importance of the flux of the ferrous complex in the redistribution of the iron inside the cell since models 2 and 4 exhibit a significant change in the total iron amount. The increase in total iron amount predicted by model 2 is higher than model 4 since in model 2, solubility of $FeCl_2$ is constant at its maximum value.

It can be concluded that although the variation in the $FeCl_2$ solubility is important, the addition of the flux of the ferrous complex into the model has a more important effect on the results.

3.4. Effect of $K_{sp,FeCl}$ on the discharge–charge cycle of the cell

The solubility product, $K_{sp,FeCl}$, has not been previously reported in the literature. Sudoh and Newman [14] assumed a constant equilibrium ferrous complex concentration of 4.1×10^{-8} mol cm^{-3} in their study. This value of $c_{r,e}$ corresponds to $K_{sp,FeCl}$ of 2.7×10^4 calculated at the saturation value of x_A according to our model. We have carried out simulations for assumed values of 10^4, 10^5, 10^6, 10^7 and 10^8. When $K_{sp,FeCl} < 10^5$, model predictions are not in accord with the previous results reported, most probably because $c_{r,e}$ is too low in the system, seriously affecting the kinetics. The results show consistent behavior for all $K_{sp,FeCl}$ values only when it is equal or higher than 10^5. $K_{sp,FeCl}$ values higher than 10^8 are not considered since the main assumption in our model is that iron chloride is sparingly soluble in the electrolyte and this range leads to too high of a concentration.

3.4.1. Effect of $K_{sp,FeCl}$ on the iron chloride volume fraction

Iron chloride volume fractions with respect to position and time for $K_{sp,FeCl}$ values of 10^5, 10^6, 10^7 and 10^8 are shown in Figs. 11 and 12, for discharge and charge, respectively. During discharge, for all $K_{sp,FeCl}$ values, the same trend is seen; ε_{FeCl} decreases with time throughout the battery and it becomes depleted for positions approaching r_L at high DODs since the reaction front migrates inwards towards the positive current collector [12]. When the curves for different solubility products are compared, it can be seen that there is a significant difference in the results only when $K_{sp,FeCl}$ is equal to 10^5 (Fig. 11). The results for the other three $K_{sp,FeCl}$ values are very similar. The difference between the 10^5 curve and the others increases with increasing DOD. For $K_{sp,FeCl}$ values of 10^6 and higher, iron chloride is depleted faster than $K_{sp,FeCl} = 10^5$ near the r_L boundary due to higher reaction rates. When comparing curves with the same DOD, a higher local transfer current at r_L must result in a lower local transfer current at r_0. Therefore the iron chloride volume fraction is lower at r_0 for $K_{sp,FeCl} = 10^5$ relative to the higher $K_{sp,FeCl}$ values.

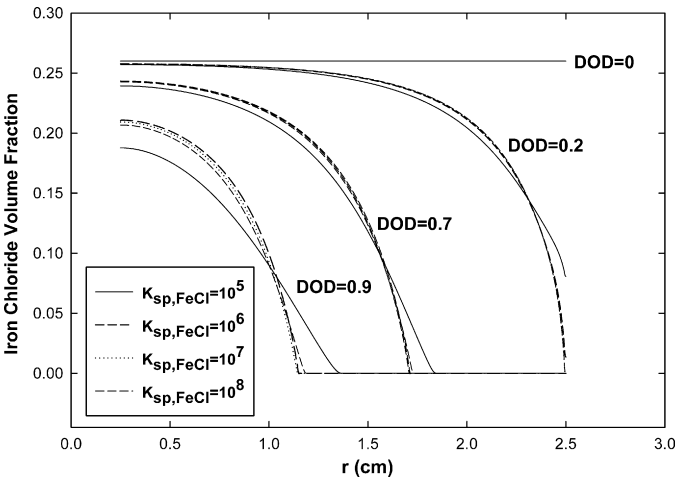

Fig. 11. Comparison of iron chloride volume fraction profiles for different $K_{sp,FeCl}$ values during discharge.

In contrast, during charge, the value of $K_{sp,FeCl}$ appears to affect behavior near the r_L boundary. As it can be seen in Fig. 12, there is a sudden decrease for ε_{FeCl} at r_L for 10^8. This result suggests that the equilibrium value of the ferrous complex has a significant effect on ε_{FeCl} at the r_L boundary when $K_{sp,FeCl}$ is higher than 10^7. This effect is not seen during discharge at the r_L boundary because $FeCl_{2(s)}$ is depleted for any value of the solubility product.

3.4.2. Effect of $K_{sp,FeCl}$ on the cell potential

The change in the cell potential with time during discharge for different values of $K_{sp,FeCl}$ can be seen in Fig. 13. The trend for all

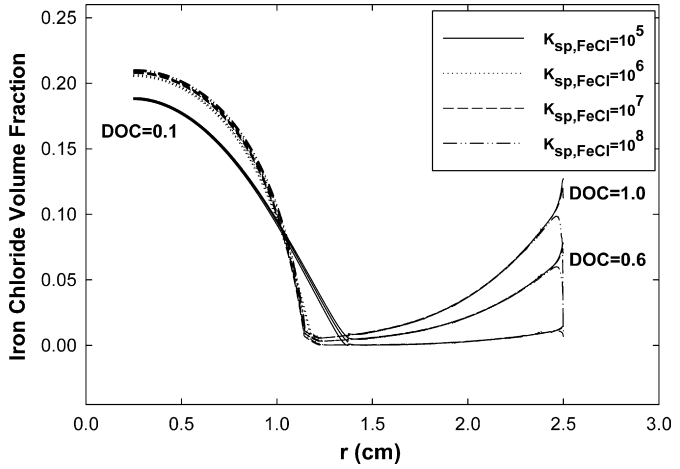

Fig. 12. Comparison of iron chloride volume fraction profiles for different $K_{sp,FeCl}$ values during charge.

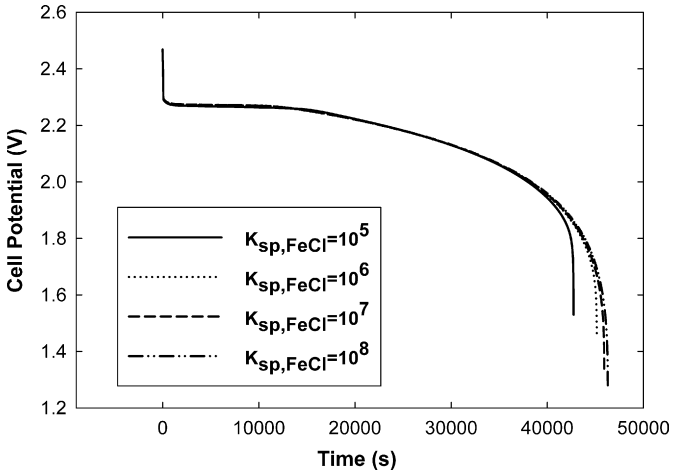

Fig. 13. Comparison of cell potentials for different $K_{sp,FeCl}$ values during discharge.

of the curves is the same; it starts with a slight decrease in the cell potential at small DODs, then a significant continuous decrease is observed, and finally at very high DODs, a very steep decrease occurs. All four curves are the same until 35,000 s. After this point there is a clear difference among the curves; they have the steep potential decrease at different times. As for the previous results, $K_{sp,FeCl} = 10^5$ has the most significant distinction from the others. The reason why the steep potential decrease is seen earlier for lower $K_{sp,FeCl}$ values can be explained by the slower kinetics at the reaction front in these systems due to the low electrolyte concentration of ferrous complex. The reaction rate at the reaction front is significantly lower for lower $K_{sp,FeCl}$ values, especially for $K_{sp,FeCl} = 10^5$. The effect of $K_{sp,FeCl}$ on the cell potential is observed only at very high DODs, suggesting that the sharp potential decrease occurs when reaction rates at the reaction front decreases to very low values. It can be seen that, in terms of the cell potential, increasing the solubility product higher than 10^7 does not have a great impact on the simulated cell potential except near the end of discharge.

3.5. Effect of continuous cycling

Continuous cycling simulations were conducted to study whether iron redistribution continued beyond the first cycle. Here, the cycling conditions are taken as discharge for 12,000 s at $-30\,mA\,cm^{-2}$ and charge for 18,000 s at $10\,mA\,cm^{-2}$. The effect of continuous cycling was investigated for five cycles.

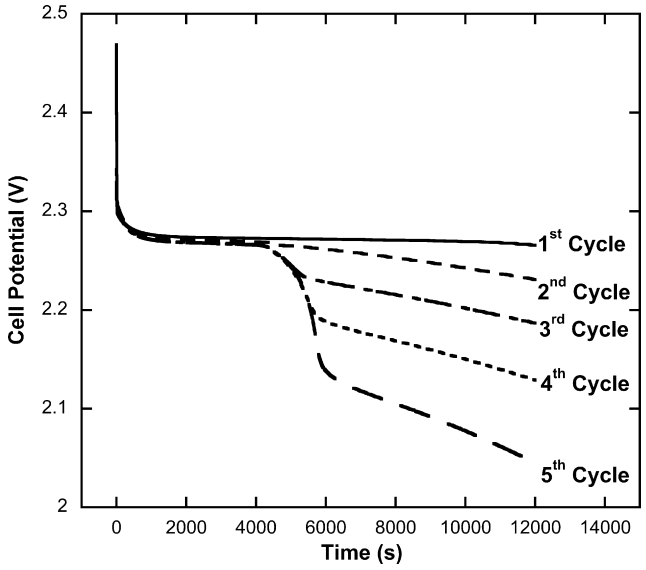

Fig. 14. The change of discharge cell potential with time for each cycle during continuous cycling ($K_{sp,FeCl} = 10^6$).

In Fig. 14, the change of cell potential with time during discharge is given for each cycle. It can be seen that under these cycling conditions, the cell potential is predicted to decrease even after 5 cycles. In addition, with cycling the trend of the potential curve also changes; there is a steep decrease in the potential at first followed by a slighter continuous decrease. This sudden potential decrease starts to occur around the same DOD at each cycle. As a result of the simulation, it has been calculated that after the 5th discharge, the cell potential decreases by nearly 10%. The change in the discharge potential curve and decline in discharge potential with continuous cycling has been reported previously [19]. The redistribution of iron inside the cathode with continuous cycling plays an important role in this potential loss. However it should be kept in mind that the discharge/charge current densities and simulation times also have a great impact on the calculated potential loss. Therefore, this extreme of potential decrease may not be seen with different cycling conditions. In addition, it has seen that cell design has a critical effect on the calculated potential loss. For instance, simulations

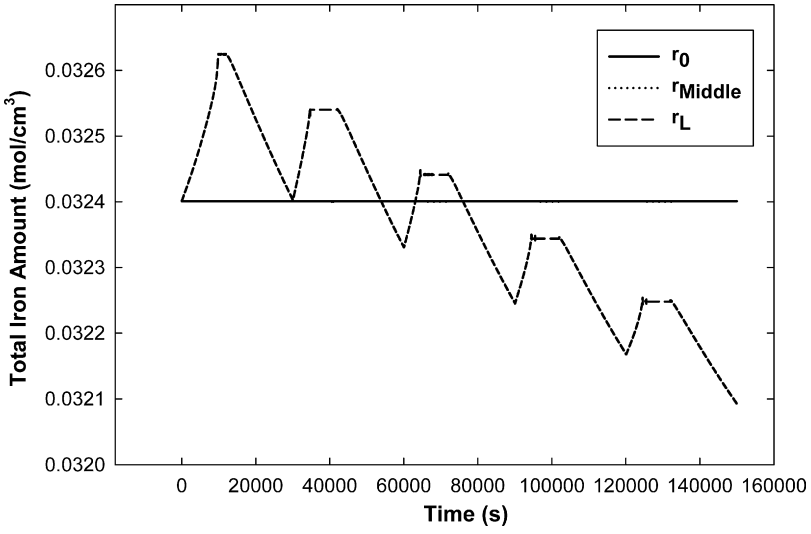

Fig. 15. The change of total iron amount with time at different radial positions during continuous cycling ($K_{sp,FeCl} = 10^6$).

suggest that the initial volume fraction ratio of iron to iron-chloride creates a significant difference in the calculated potential loss.

The change in total iron amount at r_0, r_{Middle} and r_L with continuous cycling can be seen in Fig. 15. In the previous section, a single discharge–charge cycle was investigated and, as a result of the simulations, it was seen that iron amount increases at r_L during discharge and decreases during charge. The same trends can be seen for each individual cycle in Fig. 15. As explained in the previous section, the initial increase is mainly due to the sharp increase in iron volume fraction because of the significant flux of the ferrous complex. After iron chloride is depleted, the increase in the total iron amount ends and the curve stabilizes. During charging, the ferrous complex diffuses away from r_L, causing the Fe concentration to decrease more than the $FeCl_2$ amount and the bulk concentration to increase. The figure also shows that with increased cycling, the iron depletion at r_L at the end of charging becomes more and more significant. For instance, as a result of the simulation, the total iron amount decreases by ~1% at r_L at the end of the fifth cycle. This result suggests that iron may be depleted at r_L around the end of 500th cycle causing perhaps the failure of the cell. The change in the iron amount at r_0 and r_{Middle} with continuous cycling is not as significant as the change in r_L.

Since the molar average velocity at r_L is not zero, there is a net flux of the soluble ferrous complex into the sodium tetrachloroaluminate reservoir as a result of continuous cycling. However it was calculated that the amount of iron that is lost into the reservoir due to this flux is negligible compared to the total decrease in the iron amount at this boundary. Therefore, the redistribution of iron within the electrode must be the main reason of the iron loss at r_L.

3.6. Summary and future work

Minimizing the transport and redistribution of iron inside the cathode should be considered in the cell design in order to prevent the power loss seen as a result of continuous cycling. The model proposed in this study is able to predict the iron redistribution inside the cell as a function of design parameters. For instance, it has been seen that one of the design parameters in Zebra cells, the initial ratio of iron to iron-chloride volume fraction, has a significant effect on iron redistribution inside the cell. Simulations suggest that increasing the initial ratio of iron to iron-chloride volume fraction decreases the amount of iron depleted at r_L.

The results reported in this study show that incorporation of the variation of iron chloride solubility and the flux of the ferrous complex into the model of the porous cathode is important to predict the redistribution of the metal inside the cell. For future work, the iron chloride solubility as a function of x_A would be valuable to measure directly. Furthermore the metal distribution inside the cathode at different positions at different DODs would allow for direct testing of model predictions. In addition, extending the model proposed in this paper to a $Na/NiCl_2$ cell would be of value since it is known that $Na/NiCl_2$ batteries have some superior properties over $Na/FeCl_2$ batteries, such as higher open-circuit potential [4,12].

4. Conclusions

In this study, a mathematical model for the positive cathode in a sodium–iron chloride cell with β″-alumina ceramic and molten $NaAlCl_4$/NaCl electrolyte was extended by accounting for variable solubility of $FeCl_2$. In addition to the solubility of iron chloride, this model also predicts the movement of iron inside the cell with time. It has seen that during discharge the solubility of $FeCl_2$ decreases near r_L as x_A decreases. The flux of the soluble ferrous complex becomes significant at moderate DODs leading to a non-zero electrolyte concentration of the complex although solid iron chloride is depleted near r_L. When the relocation of iron is considered, it was concluded that the net movement of iron is from r_0 to r_L during discharge, whereas the reverse happens during charge. The effect of solubility constant $K_{sp,FeCl}$ was also studied, and effects increase with increasing solubility, until 10^6. Finally, the effect of continuous cycling was examined. It was predicted that there is a deficiency of iron at r_L. As a result of the 5th cycle, there is nearly a 1% decrease in the total iron amount at the electrode–reservoir boundary.

Appendix A. Calculation of the equilibrium concentration of the ferrous complex

The equilibrium concentration of the ferrous complex is calculated using Eqs. (A1)–(A6). The concentrations of $AlCl_4^-$, Cl^- and Na^+ are all expressed in terms of x_A.

$$x_{AlCl_3} = \frac{K_M x_A}{K_2(1 - x_A)} \tag{A1}$$

$$x_{Al_2Cl_6} = K_0 x_{AlCl_3}^2 \tag{A2}$$

$$x_{Al_2Cl_7^-} = \frac{K_M x_A^2}{c_T(1 - x_A)\bar{V}_e} \tag{A3}$$

$$x_{Fe(AlCl_4)_4^{2-}} = K_{sp,FeCl} x_{Al_2Cl_7^-}^2 \tag{A4}$$

$$c_T = \frac{2}{\bar{V}_e(1 - x_{Al_2Cl_6} - x_{AlCl_3} - x_{Al_2Cl_7^-} - x_{Fe(AlCl_4)_4^{2-}})} \tag{A5}$$

$$c_{r,e} = c_T x_{Fe(AlCl_4)_4^{2-}} \tag{A6}$$

References

[1] J. Coetzer, Journal of Power Sources 18 (1986) 377–380.
[2] R.J. Bones, J. Coetzer, R.C. Galloway, D.A. Teagle, Journal of the Electrochemical Society 134 (1987) 2379–2382.
[3] R.C. Galloway, Journal of the Electrochemical Society 134 (1987) 256–257.
[4] J.L. Sudworth, Journal of Power Sources 51 (1994) 105–114.
[5] P.A. Nelson, Journal of Power Sources 29 (1990) 565–577.
[6] B.V. Ratnakumar, A.I. Attia, G. Halpert, Journal of Power Sources 36 (1991) 385–394.
[7] J.L. Sudworth, Philosophical Transactions of the Royal Society A: Mathematical, Physical and Engineering Sciences 354 (1996) 1595–1612.
[8] A. Van Zyl, Solid State Ionics 86–88 (1996) 883–889.
[9] J.L. Sudworth, Journal of Power Sources 100 (2001) 149–163.
[10] C.H. Dustmann, Journal of Power Sources 127 (2004) 85–92.
[11] T.M. O'Sullivan, C.M. Bingham, R.E. Clark, International Symposium on Power Electronics, Electrical Drives, Automation and Motion (SPEEDAM), Italy, 2006.
[12] X. Lu, G. Xia, J.P. Lemmon, Z. Yang, Journal of Power Sources 195 (2010) 2431–2442.
[13] M.A. Vallance, R.E. White, Comsol Conference, Boston, 2008.
[14] M. Sudoh, J. Newman, Journal of the Electrochemical Society 137 (1990) 876–883.
[15] R.J. Bones, D.A. Teagle, S.D. Brooker, F.L. Cullen, J. Lumsdon, 2nd Symposium on Electrode Materials and Processes for Energy Conversion and Storage, Philadelphia, 1987, p. 537.
[16] I. Bloom, P.A. Nelson, L. Redey, S.K. Orth, C.L. Hammer, R.S. Skocypec, D.W. Dees, M.C. Hash, D.R. Vissers, Proc. of 25th Intersoc. Energy Conversion Eng. Confer., vol. 3, Reno, NV, August 12–17, 1990, pp. 341–347.
[17] L.G. Boxall, H.L. Jones, R.A. Osteryoung, Journal of the Electrochemical Society 121 (1974) 212–219.
[18] R.J. Bones, D.A. Teagle, S.D. Brooker, F.L. Cullen, Journal of the Electrochemical Society 136 (1989) 1274–1277.
[19] J.S. Weaving, S. Walter Orchard, Journal of Power Sources 36 (1991) 537–546.
[20] G. Ning, B.N. Popov, Journal of the Electrochemical Society 151 (2004).
[21] K. Li, J. Wu, Y. Jiang, Z. Hassan, Q. Lv, L. Shang, D. Maksimovic, Proc. of ISLPED, 2010, pp. 277–282.
[22] R.E. Garcia, Y.M. Chiang, W.C. Carter, P. Limthongkul, C.M. Bishop, Journal of the Electrochemical Society 152 (2005).
[23] M. Doyle, T. Fuller, J. Newman, Journal of the Electrochemical Society 140 (1993) 1526–1533.
[24] G.G. Botte, V.R. Subramanian, R.E. White, Electrochimica Acta 45 (2000) 2595–2609.
[25] B. Paxton, J. Newman, Journal of the Electrochemical Society 144 (1997) 3818–3831.
[26] Y.Y. Wang, M.R. Lin, C.C. Wan, Journal of Power Sources 13 (1984) 65–74.
[27] V.J. Farozic, G.A. Prentice, Journal of Applied Electrochemistry 21 (1991) 767–773.

[28] S.W. Orchard, J.S. Weaving, Journal of Applied Electrochemistry 23 (1993) 1214–1222.
[29] J. Newman, W. Tiedemann, AIChE Journal 21 (1975) 25–41.
[30] R. Pollard, J. Newman, Journal of the Electrochemical Society 126 (1979) 1713–1717.
[31] L.G. Boxall, H.L. Jones, R.A. Osteryoung, Journal of the Electrochemical Society 120 (1973) 223–231.
[32] J. Newman, K.E. Thomas-Alyea, Electrochemical Systems, 3rd ed., Wiley-Interscience, Hoboken, 2004.